

Reprocessing from highly ionized gas in the soft spectral state of V4641 Sgr with *NuSTAR*

RILEY M. T. CONNORS,¹ JOEY NEILSEN,¹ AARRAN W. SHAW,² JAMES F. STEINER,³ FEDERICO VINCENTELLI,^{4,5}
JAVIER A. GARCÍA,^{6,7} PHIL UTTLEY,⁸ RON REMILLARD,⁹ AND GUGLIELMO MASTROSERIO¹⁰

¹*Department of Physics, Villanova University, 800 Lancaster Avenue, Villanova, PA 19085, USA*

²*Department of Physics and Astronomy, Butler University, 4600 Sunset Ave, Indianapolis, IN 46208, USA*

³*Harvard-Smithsonian Center for Astrophysics, 60 Garden St., Cambridge, MA 02138, USA*

⁴*Instituto de Astrofísica de Canarias, E-38205, La Laguna, Tenerife, Spain*

⁵*Departamento de Astrofísica, Universidad de La Laguna, E-38206 La Laguna, Tenerife, Spain*

⁶*NASA Goddard Space Flight Center, 880 Greenbelt Rd, Greenbelt, MD 20771, USA*

⁷*Cahill Center for Astronomy and Astrophysics, California Institute of Technology, 1216 E California Blvd, Pasadena, CA 91125, USA*

⁸*Anton Pannekoek Institute, University of Amsterdam, Science Park 904, Amsterdam, Netherlands*

⁹*MIT Kavli Institute for Astrophysics and Space Research, 70 Vassar St., Cambridge, MA 02139, USA*

¹⁰*Dipartimento di Fisica, Università degli Studi di Milano, Via Celoria 16, I-20133 Milano, Italy*

(Accepted by ApJ on Feb 27 2025)

ABSTRACT

V4641 Sgr is a low-mass black hole X-ray binary system with somewhat puzzling spectral characteristics during its soft state. Recent high-resolution spectroscopic studies of V4641 Sgr have revealed strong ionized emission line features in both the optical and X-ray bands, including P-Cygni signatures, and an unusually low soft state luminosity, indicating that the central engine is obscured. Here we present an analysis of five *NuSTAR* observations of V4641 Sgr taken during its recent outburst in 2021, when the source was in the soft state. We identify highly ionized Fe K emission lines, consistent with a combination of the near-neutral 6.4 keV Fe K α line, and the H-like and He-like Fe K α and Fe K β transitions found at 6.7–7 keV and \sim 8 keV, and find no evidence for strong relativistic broadening. The line fluxes correlate linearly with the observed disk continuum flux, implying a direct connection between the central engine and the reprocessing region. Most interestingly, all five spectra also show a persistent highly ionized Fe K continuum edge feature at \sim 9 keV with a stable optical depth, which is likely smeared, implying a localized reprocessing zone. We find tentative supporting evidence for obscuration of the inner accretion disk based on its unusually low intrinsic luminosity, however, the *NuSTAR* spectra do not require obscuration from cold, optically thick gas.

Keywords: accretion, accretion disks – atomic processes – black hole physics

1. INTRODUCTION

Galactic black hole (BH) transients are X-ray binary systems formed of a BH and a stellar companion. BH binaries in which the stellar companion is low mass are referred to as BH low-mass X-ray binaries (BH-LMXBs). These are evolved binary systems with orbits tight enough such that the companion star is filling its Roche lobe, causing matter to transfer onto the BH. This

process, called accretion, results in the release of powerful emission, since a significant fraction of the available gravitational energy is converted into thermal and kinetic energy in the accreting gas. BH-LMXBs spend the majority of their lifetimes in periods (years to decades) of quiescence, dim states in which the accretion rate is low, and thus the radiative luminosity (or power) is many orders of magnitude below the Eddington limit—the theoretical upper bound on luminosity imposed by the competing gravitational and radiative forces. When outbursts occur, BH-LMXBs typically increase in luminosity by several orders of magnitude on timescales of days to weeks. They often present with distinct spectral

and time-variability properties in the X-ray band which has been the basis for classifying distinct spectral states, broadly termed ‘hard’ and ‘soft’, with intermediate subdivisions (see, e.g., Homan & Belloni 2005; Remillard & McClintock 2006).

During hard spectral states the broadband X-ray spectra of BH-LMXBs are power-law distributed, with photon index $\Gamma \sim 1.5\text{--}2$, and peak X-ray luminosities of $\sim 10\% L_{\text{Edd}}$ (Remillard & McClintock 2006; Done et al. 2007). When transitioning to the soft spectral state, where a blackbody disk continuum instead dominates the spectrum, BH-LMXBs can reach luminosities $L_X \geq L_{\text{Edd}}$. Soft states are also notable for the weakness or absence of the strong fast variability and compact radio jet emission that characterize hard states in BH-LMXBs (see, e.g., Muñoz-Darias et al. 2011; Fender & Gallo 2014). Instead, the soft state is often accompanied by strong outflows that are termed accretion disk winds, distinct from jets in that they likely originate from the outer regions of the accretion flow, and are slower and less collimated than jets (see, e.g., Ponti et al. 2012).

Signatures of disk winds are typically detected spectroscopically, from near-infrared through to X-ray wavelengths, as ionized absorbers. These winds are seen in high inclination systems only, and thus likely have an equatorial geometry, such that we can only detect their absorption signatures when the accretion flow is edge on (Díaz Trigo et al. 2006; Miller et al. 2006; Ponti et al. 2012). Earlier wind studies indicated that disk winds are preferentially observed during the soft state, and thus that winds appear when the radio jet is suppressed (Miller et al. 2006; Neilsen & Lee 2009; Ponti et al. 2012, 2016), however, later studies have shown that winds can still appear alongside the jet (King et al. 2015; Muñoz-Darias et al. 2016; Homan et al. 2016).

The primary X-ray spectral identifiers of disk winds are blue-shifted absorption lines (via highly ionized H-like and He-like transitions; Lee et al. 2002; Ueda et al. 2004; Miller et al. 2006, 2008). High-resolution spectroscopic observations of these winds, in both the optical and X-ray wavebands, allow us to measure various wind properties, in particular to derive the outflow velocity. It is also possible in some cases to identify emission that is scattered out of our line of sight via the detection of strong emission lines with clear P-Cygni profiles (Brandt & Schulz 2000; King et al. 2015; Muñoz-Darias et al. 2016, 2018). Such measurements suggest a spherical geometry for the obscuring material, such that we are able to observe reprocessed emission from the obscured central source of photons, i.e., the inner accretion flow. V4641 Sgr, the BH-LMXB that is the focus of this study, is one such source in which emission line

features have been observed and analyzed in detail via high-resolution spectroscopy in both the optical and X-ray bands (Muñoz-Darias et al. 2018; Shaw et al. 2022).

1.1. V4641 Sgr

Optical studies in quiescence show the central compact object of V4641 Sgr is a BH of mass $M_{\text{BH}} = 6.4 \pm 0.6 M_{\odot}$, with a B9III (post main-sequence) companion star of mass $M_2 = 2.9 \pm 0.4 M_{\odot}$, at a distance of $D = 6.2 \pm 0.7$ kpc, binary inclination $i = 72 \pm 4$ deg, and with an orbital period of ~ 2.8 days (Orosz et al. 2001; MacDonald et al. 2014). V4641 Sgr is in a unique position as a BH-LMXB due to several of its behavioral characteristics. Since its discovery as a bright Galactic X-ray source in 1999 (in ‘t Zand et al. 1999; in ‘t Zand et al. 2000), it has undergone outbursts that vary significantly in duration and peak luminosity with a recurrence time of ~ 220 days (Tetarenko et al. 2016).

The 1999 outburst of V4641 Sgr was both rapid and bright, with the X-ray flux rising to > 12 Crab within just 8 hours, before fading over two orders of magnitude down to ~ 0.2 Crab within 2 hours (Smith et al. 1999; Hjellming et al. 2000). Further analysis of the available data suggested that the source was in a super-Eddington state during this time, and that the disk continuum emission may be obscured, enshrouded in an envelope (Revnivtsev et al. 2002). Subsequent outbursts have been comparatively stunted, with longer, fainter periods of X-ray activity. Furthermore, V4641 Sgr is seen to remain in a soft, disk-dominated spectral state down to much lower Eddington-scaled luminosities (as low as $6 \times 10^{-4} L_{\text{Edd}}$; Bahramian et al. 2015) than typical (Dunn et al. 2010).

Analysis of *Chandra* High Energy Transmission Grating (HETG) spectra from observations of the 2020 outburst of V4641 Sgr revealed a rich set of ionized emission lines atop a strongly scattered disk continuum, and showed that there is likely more than one photoionization region surrounding the central engine (Shaw et al. 2022). Further analysis, together with spectral data from the *Nuclear Spectroscopic Telescope Array* (*NuSTAR*; Harrison et al. 2013), demonstrated that the central engine is obscured. The low energy coverage of *Chandra* required a partial covering gas to be adequately modeled, with some evidence for weak P-Cygni line profiles (blue absorption and red emission components). These factors led Shaw et al. (2022) to conclude there may be a spherical geometry to the surrounding material, though they did not specifically model this geometry, and the blue-shifted absorption features were not detected with high statistical significance.

V4641 Sgr underwent an X-ray brightening in 2021, and was detected by the *Monitor of All-Sky X-ray Image* (MAXI; Matsuoka et al. 2009) Gas Slit Camera (GSC; Mihara et al. 2011) alert system in October 2021 (Negoro et al. 2021). It was shown to have begun rising in flux as early as August 2021, and had reached a 2–10 keV flux of ~ 20 mCrab as of October 12 2021. Follow up observations with the *INTErnational Gamma-Ray Astrophysics Laboratory* (INTEGRAL; Winkler et al. 2003), the *Neil Gehrels Swift Observatory* (*Swift*; Gehrels et al. 2004) X-ray Telescope (XRT; Burrows et al. 2005) and the *Neutron Star Interior Composition Explorer* (*NICER*; Gendreau et al. 2012), confirmed the X-ray brightening (Motta et al. 2021). Further *NICER* observations on October 13, 14 and 16 revealed more details about the source (Buisson et al. 2021): V4641 Sgr was varying slightly in flux day-to-day, between ~ 15 and ~ 20 mCrab, and showed a strong spectral turnover in the 2–10 keV band of *NICER*, consistent with a soft thermal disk blackbody spectrum with inner disk temperature $kT_{\text{in}} \sim 1.3$ keV. Most interestingly, *NICER* detected prominent emission line features in the iron K band of the X-ray spectrum (6.7–7 keV). Buisson et al. (2021) reported that by stacking the *NICER* spectra they were able to detect a double-peaked line shape in the iron K band, with centroids at ~ 6.7 keV and ~ 6.97 keV, which corresponds to the He-like and H-like ionized Fe K α lines (Fe XXV and Fe XXVI). Furthermore, they report that they do not detect statistically significant changes to the line properties (across the three *NICER* observations, a 4-day window), despite moderate variations in the X-ray continuum, potentially indicating some evolution in either the geometry or ionization structure of the emission line region.

NuSTAR initially observed V4641 Sgr on October 15 2021 as part of a Target-of-Opportunity (ToO) Guest Observer (GO) program. The source was observed a total of five times over a month-long period (see Figure 1): the first four observations were spaced a few days apart and spanned ~ 2 weeks before a ~ 2 week gap, upon which the fifth snapshot was taken. Each snapshot lasted ~ 20 ks.

1.2. This Work

In this paper we present broadband X-ray spectral modeling of the five *NuSTAR* observations of V4641 Sgr in October–November 2021, during which the source was in a soft spectral state, with a bright disk component and a faint power law tail, as well as several ionized emission lines and an apparent absorption edge feature at ~ 9 –10 keV. In Section 2 we discuss the data reduc-

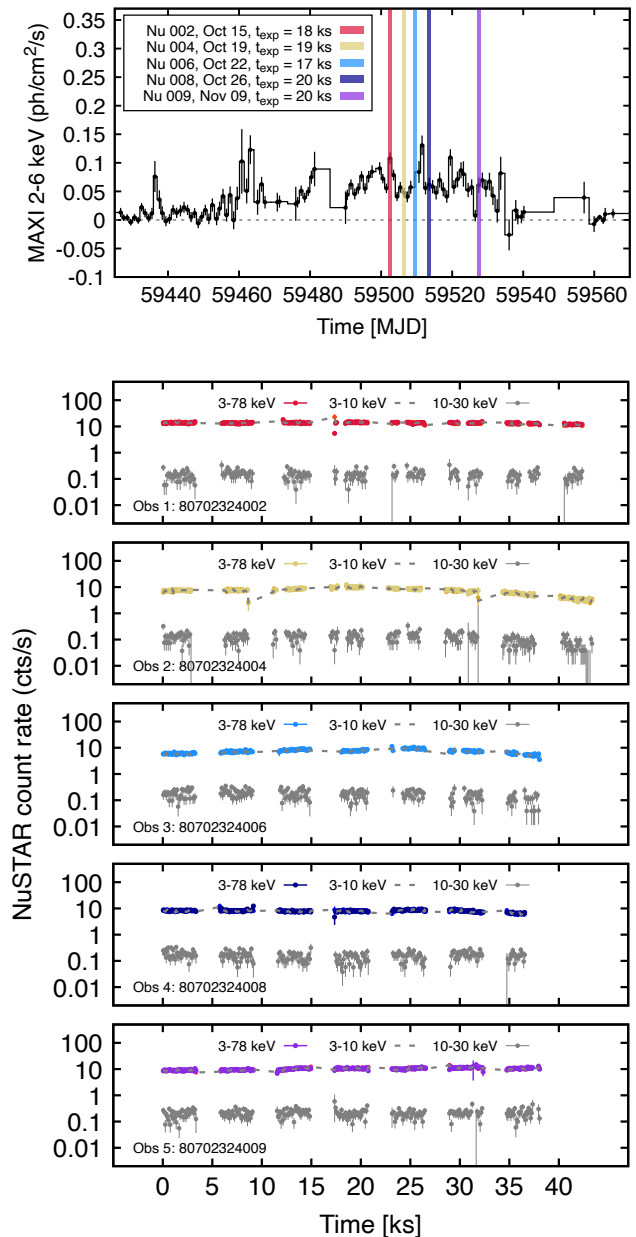


Figure 1. **Top:** the long term MAXI light curve of V4641 Sgr. The colored bars indicate the *NuSTAR* observation times associated with our study, with ObsID 80702324. **Bottom:** the five individual *NuSTAR* light curves, in 100s bins. Each panel shows the color-coded 3–78 keV rates, plus the soft and hard band count rates in gray dashed lines and points respectively, showing that the source is dominated by variable (long-term) soft emission.

tion and analysis, in Section 3 we present the results of comprehensive spectral modeling of all five *NuSTAR* observations of V4641 Sgr, and in Section 4 we discuss the implications of our results, with a particular focus

on the ionized Fe K complex and the disk continuum constraints.

2. OBSERVATIONS AND DATA REDUCTION

The long-term MAXI light curve of V4641 Sgr is shown in Figure 1, with the five *NuSTAR* observation periods overplotted, and individual *NuSTAR* light curves in sequential panels. The ObsID is 80702324 with appended Sequence IDs 002, 004, 006, 008, and 009. We have included full band (3–78 keV), soft band (3–10 keV) and hard band (10–30 keV) light curves, which demonstrate that the source is in a soft state with power law flux on the few % level. A rudimentary check of the short term variability of the source (by generating power spectra from all 5 observation light curves) reveals only Poisson noise, i.e., there is no short term variability across the entire *NuSTAR* passband.

We performed data reduction on all five *NuSTAR* observations in an identical manner. All data processing was performed using `HEASoft v6.30.1`, `nustardas v2.1.2` and the most recent *NuSTAR* calibration database (CALDB) at the time of analysis, v20221019 released on October 19 2022. Initially we processed all five observations using `nupipeline` with default settings. Despite V4641 Sgr being a bright Galactic X-ray source, we did not process the data using the bright status flag¹ since a rudimentary scan of the light curves (in 1s bins) showed the total observed count rate consistently remained below 100 cts s⁻¹.

We then used `DS9 SAOIMAGE` (Joye & Mandel 2003) to select the source and background regions prior to extracting data products. *NuSTAR* has two focal plane modules (FPM A and B) each comprised of four 32 × 32 pixel detectors arranged in a 2 × 2 square grid (Det 0, Det 1, Det 2, and Det 3, clockwise). A prominent stray light source is present in both FPMs, and sits on the same detector (Det #0) upon which the source is located. We therefore extracted the background spectrum from Det #2. We extracted source spectra and light curves for FPMs A and B (using `nuproducts`) from a circular region of 60" centered on the source, and selected a background of the same size in our chosen off-source region. We group all data with a minimum $S/N = 5$, and only include data between 3 and 79 keV. In the analysis that follows we adopt Cash statistics throughout, given the low count rates at high energies (see Figure 2).

3. SPECTRAL MODELING

Here we outline our full spectral analysis of the *NuSTAR* observations of V4641 Sgr. We performed all our

spectral analysis using the Interactive Spectral Interpretation System (ISIS; Houck & Denicola 2000) version 1.6.2-51. V4641 Sgr was in a soft spectral state throughout the five *NuSTAR* observations from mid-October to mid-November 2021. Figure 2 shows the binned FPM A counts data for all five observations, and the statistical residuals of a simple absorbed multitemperature disk blackbody fit to the spectra. We adopt the model `TBabs*(diskbb)`, where `TBabs` is the model for photoelectric absorption in the interstellar medium (we use the atomic abundances of Wilms et al. 2000 and Verner et al. 1996 cross sections), and `diskbb` represents a multitemperature disk blackbody (Mitsuda et al. 1984; Makishima et al. 1986; Kubota et al. 1998). We fix the hydrogen column density to $N_{\text{H}} = 2.5 \times 10^{21} \text{ cm}^{-2}$ based on previous *NICER* and *NuSTAR* X-ray spectral analysis of V4641 Sgr (Pahari et al. 2015; Shaw et al. 2022). The residuals show clear, prominent spectral features beyond a simple disk continuum: (i) a weak power law tail at high energies; (ii) ionized emission features in the 6–7 keV region, and potentially at ~ 8 keV as well; and (iii) an apparent dip in the spectral continuum in the 8–12 keV region. In addition, all these spectral features appear to be at a similar counts ratio with respect to the underlying continuum model, i.e., roughly constant equivalent width (see Figure 3). The disk continuum evolves slightly over the several week long observation period: the inner disk temperature varies by $\sim 10\%$ from ~ 1.3 – 1.45 keV and disk normalization varies by a factor of 2–3 from ~ 8 – 18 .

The line features are likely associated with ionized iron $K\alpha$ and $K\beta$ emission (Shaw et al. 2022). The dip at higher energies, however, is of unknown origin. Shaw et al. (2022) note that an edge feature at ~ 9.5 keV allows a good fit to their *NuSTAR* data, but do not speculate on its origin. Pahari et al. (2015) suggest that the emission line feature at ~ 8 keV is associated with nickel, and that the 9.5 keV feature is a strong narrow edge, possibly also nickel. Here we explore these spectral features and the underlying broadband continuum of V4641 Sgr with step-by-step modeling.

We start by adding a thermal Comptonization model, `nthComp` (Zdziarski et al. 1996; Życki et al. 1999), to account for the excess high energy emission beyond ~ 10 keV. The `nthComp` model calculates the inverse Compton up-scattering of a distribution of seed multitemperature blackbody photons from the accretion disk, with the inner disk temperature set to the value of kT_{in} from the `diskbb` component. The scattering particles are hot electrons originating from the coronal plasma, the geometry/size of which we leave ambiguous. The electrons follow a thermal Maxwellian with temperature

¹ https://heasarc.gsfc.nasa.gov/docs/nustar/nustar_faqs.html

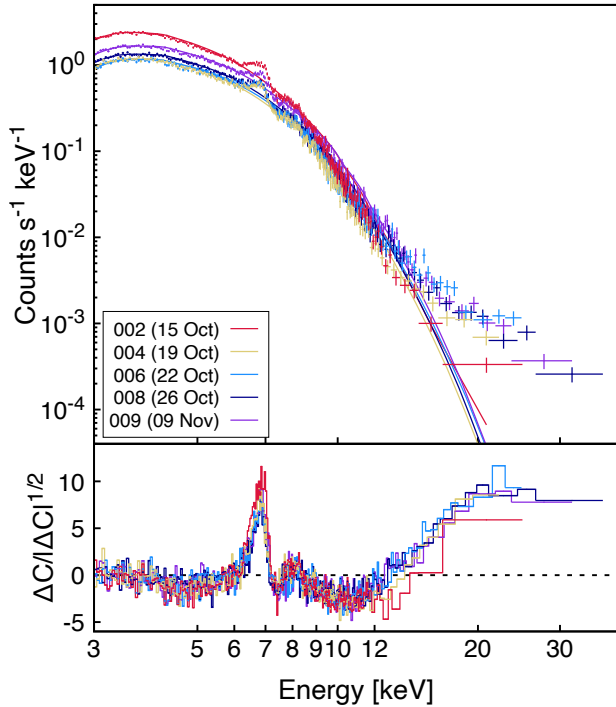


Figure 2. Summary of all five *NuSTAR* observations (FPM A only) of V4641 Sgr during a month-long period in its 2021 outburst, fit with the model $\text{TBabs}^*(\text{diskbb})$. **Top:** Counts data for all five observations. Overplotted lines show the model fit to each spectrum. **Bottom:** Cash statistic residuals.

kT_e , which we fix to 100 keV, given the lack of visible high energy cutoff. The fit of this absorbed disk+corona continuum model ($\text{TBabs}^*(\text{diskbb}+\text{nthComp})$) is shown in the top panels of Figure 3 as data/model ratios. The subsequent four plot panels then show our model progression.

In the following subsections (3.1 and 3.2) we discuss the line and edge features in more detail.

3.1. Fe Emission Lines

Atop the underlying continuum we add a succession of emission line components in the form of Gaussian models (Figure 3), starting with the most prominent residual feature at $\sim 6.5\text{--}7$ keV, likely associated with the ionized Fe $K\alpha$ lines between 6.7–6.97 keV. We allow a broad range for the centroid energy so as not to bias the fit, but for each spectrum its value settles close to 6.84 keV, which is equidistant from both the ionized Fe XXV and Fe XXVI transition energies (6.7 and 6.97 keV). *NuSTAR* does not have sufficient energy resolution (~ 400 eV at 10 keV) to distinguish these features. The second panel of Figure 3 shows this spectral fit, where it is evident that a single narrow line component is insufficient to model all the 6–7 keV features.

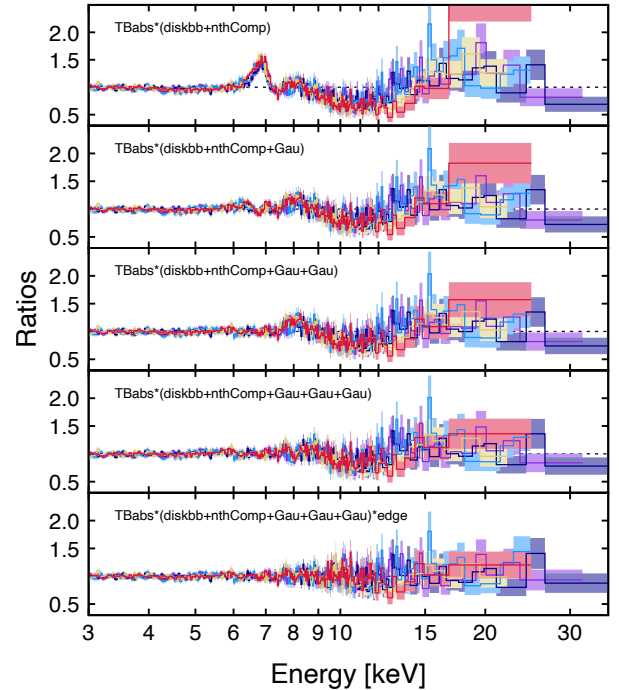


Figure 3. Residuals resulting from a step-by-step progression of model fits to all five *NuSTAR* observations of V4641 Sgr. Each successive model contains one additional component, such that the first model is the baseline continuum consisting of absorbed disk+Comptonization components, followed by three additional Gaussians in turn (the ~ 6.4 keV neutral Fe $K\alpha$ line, the ionized Fe $K\alpha$ line between 6.7–6.97 keV, and the ionized Fe $K\beta$ line at $\sim 7.88\text{--}8.25$ keV), and finally an edge component at ~ 9.5 keV.

We therefore add an additional Gaussian component at ~ 6.4 keV, once again allowing a broad range for the centroid energy when fitting. We add a final emission line component at ~ 8 keV to account for excess residuals there, likely associated with Fe XXV and Fe XXVI $K\beta$. We fix the line widths to $\sigma = 100$ eV based on preliminary fits to each observation and the results of Shaw et al. (2022), and to avoid blending the individual components by allowing too much freedom. We do not see evidence for strong relativistically broadened Fe K emission, in contrast with previous results focused on analysis of *NuSTAR* observations taken in 2014 (Pahari et al. 2015).

Figure 4 shows the dependence of the three modeled Fe emission line energies on the disk continuum flux. Whilst the energies of all three Gaussian line components remain relatively stable, there is a mild dependence on disk flux, particularly in the case of the neutral Fe $K\alpha$ and blended ionized Fe $K\alpha$ lines at ~ 6.4 keV and ~ 6.8 keV respectively. This difference is clear when comparing the lowest and highest flux observations: the neutral Fe $K\alpha$ component appears to shift

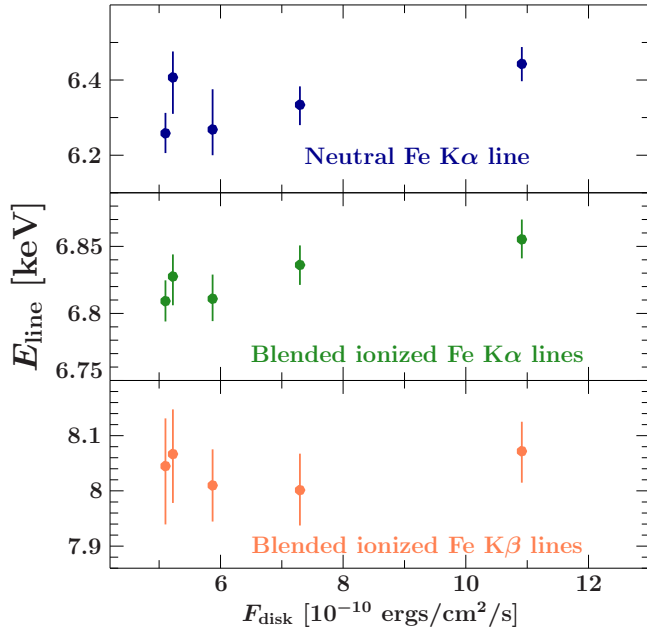


Figure 4. Gaussian line energies versus disk continuum flux for all five spectra fit with model 1: $\text{TBabs}*(\text{diskbb}+\text{nthComp}+\text{Gau}+\text{Gau}+\text{Gau})*\text{edge}$. The neutral Fe $K\alpha$ line at ~ 6.4 keV and the ionized Fe $K\alpha$ lines at ~ 6.83 keV appear to correlate with increasing disk flux.

from ~ 6.25 keV up to ~ 6.45 keV, while the blended ionized Fe $K\alpha$ component shifts from ~ 6.81 keV up to ~ 6.85 keV. These shifts are relatively minor but, particularly in the case of the ionized component, the increase in energy may reflect an increased relative flux in the 6.97 keV Fe XXVI component (see Figure 5). If true, this would indicate an increase in the ionization of the reprocessing region. Such an increase would be expected since the disk flux differs by a factor ~ 2 throughout the observing period, indeed the line shift is visible between observations 1 and 3 shown in Figure 5, which differ in continuum flux by a factor of 2.

3.2. Ionized Edge Feature: Testing Models

In order to unambiguously verify the edge feature (included in the fit shown in the bottom panel of Figure 3), we next explore a variety of continuum models and assess the effect of such model variations on the spectral features. We chose a series of five source continuum models to perform this test, each expected to produce slight differences in the shape of either the disk continuum or Comptonization continuum, or both. The continuum constituents of the models are as follows:

- Model 1: `thcomp*diskbb`
- Model 2: `thcomp*ezdiskbb`
- Model 3: `thcomp*kerrbb`

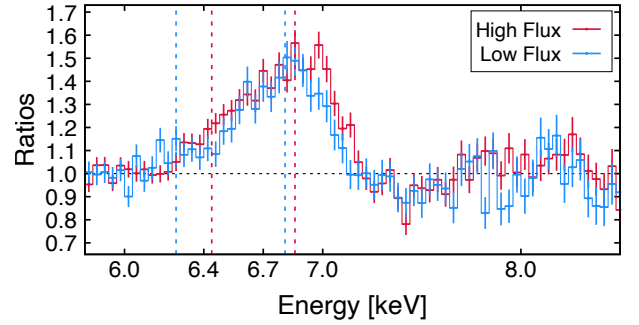


Figure 5. A comparison of ratio residuals between fits of $\text{TBabs}*\text{diskbb}$ to observations 1 and 3 (002 and 006), the former having roughly $2\times$ higher source flux than the latter. The dashed lines indicate the centroids of the neutral and ionized Fe $K\alpha$ lines resulting from the full fits of model 1 to each spectrum. The higher flux spectrum has centroids at higher energies.

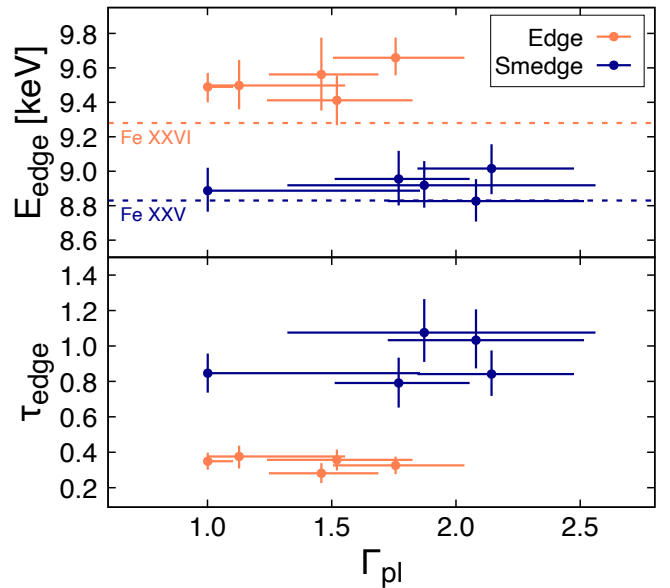


Figure 6. Edge energy and optical depth as a function of the power law photon index, Γ_{pl} , based on fit of Model 1a and Model 1b to all five spectra, Model 1a is identical to Model 1, Model 1b is a variation on Model 1 in which the `edge` model component is replaced by a smeared edge, or `smedge`, component. The two dashed lines in the upper panel indicate the Fe XXV and Fe XXVI ionization levels.

- Model 4: `thcomp*slimbh`
- Model 5: `diskpn+eqpair`

In each case, the total model is $\text{TBabs}*(\text{CONTINUUM MODEL}+\text{Gaussian}+\text{Gaussian}+\text{Gaussian})*\text{edge}$. The variations include an accretion disk with a zero-torque boundary condition (`ezdiskbb`; Zimmerman et al. 2005), a general relativistic disk around a Kerr BH (`kerrbb`; Li et al. 2005), a relativistic slim accretion disk (`slimbh`; Sadowski et al. 2011), and a hybrid

thermal/non-thermal Comptonization model (`eqpair`; Coppi 2000) with a post-Newtonian disk (`diskpn`; Gierliński et al. 1999). For Models 1–4 we have replaced the previously adopted `nthComp` model with the convolution routine `ThComp` (Zdziarski et al. 2020), which is an improvement on `nthComp` which treats scattering by mildly-relativistic electrons more accurately (more specifically, the regime $kT_e \sim E_{\text{ph}}$). We adopt `ThComp` because it is a convolution routine which we can apply to arbitrary input seed photon distribution, whereas `nthComp` assumes that input distribution is that of the `diskbb` model. We fit all five models to each spectrum, independently, with the edge feature switched on and then switched off.

We find that the edge feature cannot be subsumed by the combined disk and Comptonization continua. In fact, regardless of which model we apply, while the fit statistics vary slightly, the data-to-model ratios are almost identical. An edge feature is seemingly required by the data, and it appears between 9–10 keV; we consistently find the edge energy prefers to settle at ~ 9.5 keV. The edge feature reduces the Cash fit statistic by $\sim \Delta C = 100$ for all Models 1–5.

Despite the lack of low-energy coverage (*NuSTAR* extends down to 3 keV), previous soft X-ray spectroscopic analyses have shown that a partial covering absorber may be present in V4641 Sgr (Koljonen & Tomsick 2020; Shaw et al. 2022). It is therefore worth verifying whether or not such an obscurer could impact the appearance of the visible edge feature, in much the same way we have tested for the impacts of alternative continuum models. Since applying Models 1–5 to our data reveal no significant variations in the appearance of the edge feature, we take Model 1 and include a `TBpcf` component (Wilms et al. 2000), a commonly adopted partial covering model with two parameters, the equivalent hydrogen column (N_{H}) and a dimensionless covering fraction (f_{cov}). We allow both parameters to vary freely when fitting the data, but we find that the partial coverer only impacts the soft X-ray band below the Fe K region, i.e., it does not affect the veracity of the edge feature—the difference in Cash fit statistic is just $\Delta C/\Delta \text{DoF} = 13/2$, and the edge appears identical in the ratio residuals.

To investigate the edge feature further, we took Model 1 and replaced the `edge` model component with a `smedge` component instead, in order to make a comparison of the properties of the edge in each case. The `smedge` model is a continuum edge that has a smearing kernel applied to it, representing broadening of the feature from processes such as bulk motion of the reprocessing material, or relativistic smearing (Ebisawa 1991). The motivation behind applying the `smedge` model as

a comparison is simply that whether the reprocessing is occurring in more distant surrounding gas, or closer to the inner accretion disk, the material is likely to be in motion (Koljonen & Tomsick 2020; Shaw et al. 2022) and consisting of different ionization zones, thus one expects a certain degree of broadening to the edge feature—whether due to motion, blended features, or scattering. We fix the smearing width to $\sigma_{\text{smedge}} = 2$ keV based on preliminary fits, and to avoid degeneracies with the optical depth.

Figure 6 shows a comparison of the edge constraints (energy and optical depth) between the two model flavors 1a and 1b (`edge` vs `smedge`) as a function of the photon index of the Comptonization component, which reveals three key differences: (i) the `edge` component consistently lies at energies greater than the highest ionization continuum edge of iron, Fe XXVI, the H-like level at 9.28 keV (the constrained value is typically closer to ~ 9.5 keV), whereas the `smedge` component is broadly consistent with the Fe XXV He-like level at 8.83 keV; (ii) the optical depth of the `smedge` component is several times higher than that of the `edge` component; and (iii) the Comptonizing continuum is softer when applying the `smedge` component, and thus more consistent with what we expect in BH-LMXB soft states (Remillard & McClintock 2006).

In the following Section (3.3) we discuss full joint spectral fits to all five *NuSTAR* spectra we performed based on the demonstrated relative stability of the line and edge features.

3.3. Joint Fits

Here we present full joint spectral fits to all five *NuSTAR* observations of V4641 Sgr with key parameters tied between the models applied to each dataset. Based on the findings of our modeling of the individual spectra (see Sections 3.2 and 3.1), we selected two key models to explore in full detail with joint fits, which we name Model 1a and Model 1b:

- Model 1a: `TBabs*(diskbb+nthComp+Gau+Gau+Gau)`
* `edge`
- Model 1b: `TBabs*(diskbb+nthComp+Gau+Gau+Gau)`
* `smedge`

where the only difference lies in the choice model component to represent the continuum edge found at ~ 9 keV: `edge` vs `smedge`. In each case we tie the edge energy (E_{edge} , E_{smedge}) and optical depth (τ_{edge} , τ_{smedge}) across all fits, as well as the Gaussian line energies (E_{g1} , E_{g2} and E_{g3})—the widths of the lines are all fixed to $\sigma = 100$ eV as before, and the smeared edge

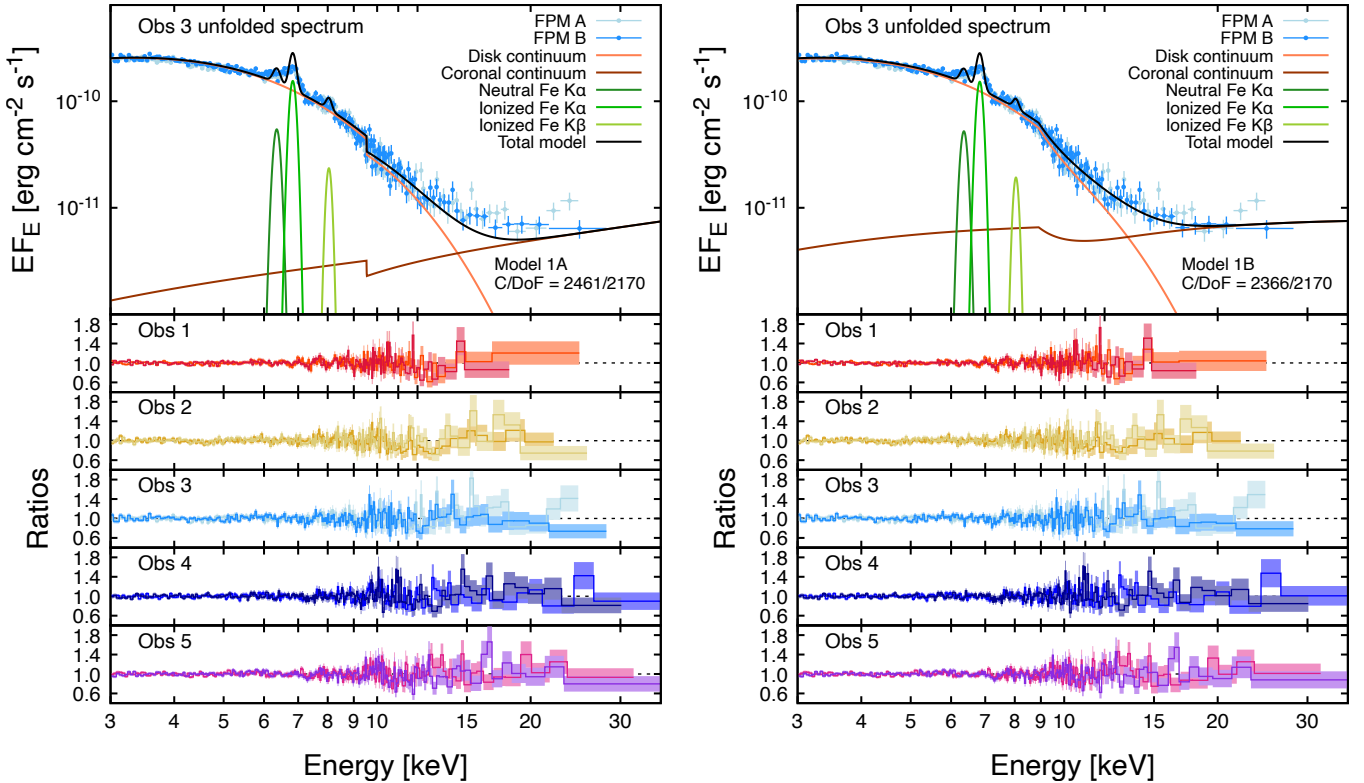


Figure 7. Unfolded flux spectrum with the associated model components and ratio residuals for each fit to the five *NuSTAR* observations of V4641 Sgr. The left panels show fits of Model 1a, right panels show fits of Model 1b. The only difference between the two models is the treatment of the absorption edge feature around ~ 9 keV: in Model 1a this feature is modeled using the edge component, in Model 1b it is instead modeled with a smeared edge or *smedge* component.

width is fixed to $\sigma_{\text{smedge}} = 2$ keV. The remaining parameters are also all treated as before, i.e., full freedom is given to the disk (kT_{in} and F_{disk}) and Comptonization (Γ and F_{pl}) components, which vary across all five spectra.

Figure 7 shows the final fits and associated residuals, and Table 1 shows the maximum likelihood estimates of the model parameters and their 90% confidence intervals. We calculated confidence intervals using the `conf_loop` parameter exploration function within ISIS, which is analogous to the `error` command typically used within `xspec`—the function loops through the free model parameters and calculates the errors, refitting the model whenever a lower fit statistic is found.

We see the same key differences in the edge energy (E_{edge} vs E_{smedge}) and optical depth (τ_{edge} vs τ_{smedge}) between models 1a and 1b as those found in our individual spectral fits, as well as the power law continuum constraint; Model 1b gives photon indices consistent with $\Gamma \sim 2$, which is typically observed in BH-LMXB soft state spectra. All other parameters are indistinguishable. Model 1b also gives an improvement in the Cash statistic of ~ 100 over Model 1a (2366 vs 2461) for the same degrees of freedom. All these factors confirm that

the observed absorption edge feature at ~ 9 keV is likely a smeared continuum edge originating from Fe XXV at 8.83 keV, i.e., we are seeing absorption of the continuum emission via highly ionized Fe in a photo-ionized gas surrounding the accretion flow which is in motion.

3.3.1. Parameter trends

Figure 8 shows the emitted photon flux (top) and equivalent width (EW; bottom) for each modeled Gaussian line (at ~ 6.35 keV, 6.83 keV, and 8.04 keV respectively) against the disk continuum flux, resulting from Model 1a fits (we choose to show only Model 1a fit results here since the trends are very similar for both Model 1a and 1b). There is a distinct positive correlation between the flux of each line and the disk continuum flux, which is confirmed by a regression line fit to each trend respectively. Interestingly, the EWs are also quite stable, showing no correlation with disk flux, though there are some variations around the mean value. This shows there is likely a connection between the observed disk continuum emission and the reprocessed line emission, i.e., we must be seeing at least some portion of what the photoionized gas sees.

Table 1. Maximum likelihood estimates and 90% confidence intervals of all parameters in spectral fitting the five *NuSTAR* observations of V4641 Sgr with Model 1a (TBabs*(diskbb+nthComp+Gau+Gau+Gau)*edge) and Model 1b (TBabs*(diskbb+nthComp+Gau+Gau+Gau)*smedge)

Parameters	Model 1a				
C/DoF	2461/2170				
N_{H} [10^{22} cm $^{-2}$]	0.25 ^a				
E_{g1} [keV]	6.35 ± 0.03				
E_{g2} [keV]	6.829 ± 0.007				
E_{g3} [keV]	8.04 ± 0.03				
E_{edge} [keV]	9.54 ^{+0.05} _{-0.06}				
τ_{edge}	0.33 ± 0.02				
	Obs 1	Obs 2	Obs 3	Obs 4	Obs 5
kT_{in} [keV]	1.263 ± 0.005	1.332 ± 0.008	1.38 ± 0.01	1.345 ^{+0.009} _{-0.008}	1.366 ± 0.008
Γ	< 1.09	< 1.4	1.5 ± 0.3	1.5 ± 0.2	1.7 ^{+0.3} _{-0.2}
F_{g1} [10^{-4} Ph cm $^{-2}$ s $^{-1}$]	2.9 ± 0.4	1.6 ± 0.3	2.1 ± 0.3	1.3 ± 0.3	2.0 ± 0.3
F_{g2} [10^{-4} Ph cm $^{-2}$ s $^{-1}$]	9.7 ± 0.4	5.3 ± 0.3	5.1 ± 0.3	4.6 ± 0.3	5.8 ± 0.3
F_{g3} [10^{-4} Ph cm $^{-2}$ s $^{-1}$]	1.4 ± 0.2	0.7 ± 0.2	0.6 ± 0.2	0.6 ± 0.2	0.8 ± 0.2
F_{disk} [10^{-10} erg cm $^{-2}$ s $^{-1}$]	10.92 ± 0.07	5.24 ± 0.04	5.12 ± 0.04	5.86 ± 0.04	7.29 ± 0.05
F_{pl} [10^{-10} erg cm $^{-2}$ s $^{-1}$]	0.5 ^{+0.1} _{-0.4}	0.3 ^{+0.8} _{-0.2}	0.31 ^{+0.12} _{-0.05}	0.24 ^{+0.05} _{-0.03}	0.23 ^{+0.03} _{-0.02}
Parameters	Model 1b				
C/DoF	2366/2170				
N_{H} [10^{22} cm $^{-2}$]	0.25 ^a				
E_{g1} [keV]	6.35 ± 0.03				
E_{g2} [keV]	6.827 ± 0.007				
E_{g3} [keV]	8.04 ^{+0.03} _{-0.04}				
E_{smedge} [keV]	8.91 ± 0.06				
τ_{smedge}	0.89 ± 0.06				
	Obs 1	Obs 2	Obs 3	Obs 4	Obs 5
kT_{in} [keV]	1.273 ^{+0.005} _{-0.006}	1.33 ± 0.01	1.37 ± 0.01	1.35 ± 0.01	1.37 ± 0.01
Γ	< 2	1.6 ^{+0.5} _{-0.4}	1.9 ± 0.3	1.9 ^{+0.3} _{-0.2}	2.2 ± 0.3
F_{g1} [10^{-4} Ph cm $^{-2}$ s $^{-1}$]	2.7 ± 0.4	1.5 ± 0.3	2.0 ± 0.3	1.2 ± 0.3	1.9 ^{+0.4} _{-0.3}
F_{g2} [10^{-4} Ph cm $^{-2}$ s $^{-1}$]	9.5 ± 0.4	5.3 ± 0.3	5.0 ± 0.3	4.5 ± 0.3	5.7 ± 0.3
F_{g3} [10^{-4} Ph cm $^{-2}$ s $^{-1}$]	1.2 ± 0.2	0.7 ± 0.2	0.5 ± 0.2	0.5 ± 0.2	0.7 ± 0.2
F_{disk} [10^{-10} erg cm $^{-2}$ s $^{-1}$]	10.84 ± 0.07	5.20 ^{+0.04} _{-0.05}	5.06 ^{+0.05} _{-0.06}	5.80 ± 0.05	7.19 ^{+0.06} _{-0.07}
F_{pl} [10^{-10} erg cm $^{-2}$ s $^{-1}$]	0.6 ^{+0.2} _{-0.5}	0.18 ^{+0.13} _{-0.03}	0.31 ^{+0.03} _{-0.02}	0.26 ± 0.02	0.29 ^{+0.06} _{-0.04}

NOTE— ^aFrozen parameter.

In all fits the following parameters are frozen: $N_{\text{H}} = 2.5 \times 10^{21}$ cm $^{-2}$, $kT_{\text{e}} = 100$ keV, $\sigma_{\text{g}} = 100$ eV (Gaussian line widths), $\sigma_{\text{smedge}} = 2$ keV (the width of the smeared edge as adopted in Model 1b). In addition, we calculate the unabsorbed line and continuum fluxes using the `cpflux` and `cflux` convolution kernels respectively. We fix the integration limits of the line photon fluxes to $E_{\text{min}} = 0.5$ keV, $E_{\text{max}} = 10$ keV. The `diskbb` flux is calculated over the range 0.01–50 keV, and the `nthComp` flux over the range 0.01–200 keV.

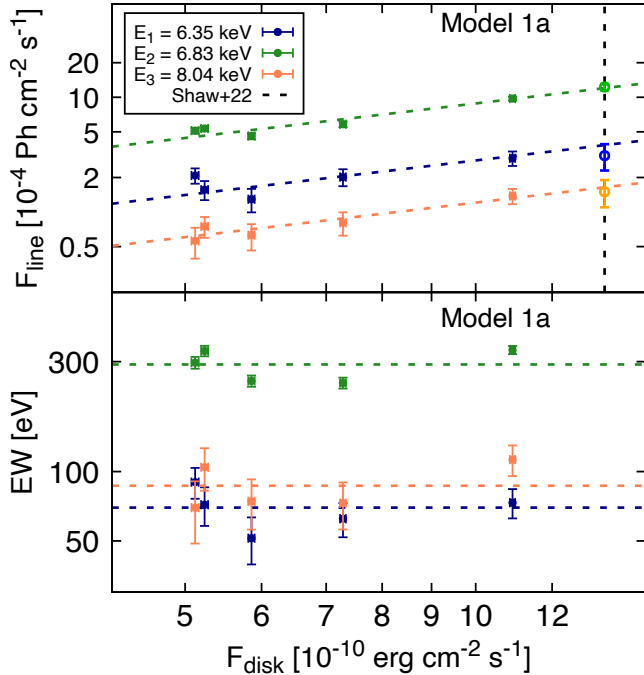


Figure 8. Top: Emission line fluxes versus the disk continuum flux for Model 1a fits. The dotted lines show fits to the trend of each emission line energy vs disk flux with a slope of 1, demonstrating a one-to-one correlation between the line and continuum fluxes. The lighter points coincident with the vertical black line show the same constraints found by Shaw et al. (2022) resulting from similar fits to earlier *NuSTAR* observations of V4641 Sgr. Note these points are overplotted and not part of the regression. **Bottom:** Line equivalent width (EW) vs disk continuum flux for all three modeled Gaussian emission lines. Dotted lines show the flat mean EW value fit to the constraints.

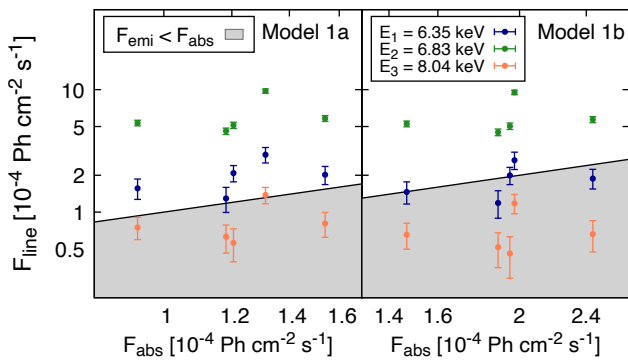


Figure 9. Emission line fluxes versus the absorbed photon flux, via the ionized iron continuum edge, showing constraints from both Model 1a (left) and Model 1b (right) fits. The shaded zone shows the region in which the emitted photon flux is less than the absorbed photon flux, which violates photon conservation (Reynolds et al. 2009).

Table 1 shows that the power law flux remains low compared to the disk flux ($F_{\text{pl}} \sim 0.05 F_{\text{disk}}$), and statistically consistent with being unchanged between observations. The power law photon index (Γ) shows some variation but is poorly constrained in all our fits—it is always consistent with a flat spectrum, $\Gamma = 2$.

Figure 9 shows the line photon fluxes against the photon flux absorbed in the edge component. We compare constraints from Models 1a (left) and 1b (right), since the *edge* and *smedge* components give different absorbed fluxes. The shaded regions indicate the phase space in which photon conservation is violated, i.e., where the number of photons emitted is less than the number absorbed by the gas ($F_{\text{emi}} < F_{\text{abs}}$), which is unphysical if we assume the line emission is re-emission from the absorbing gas (Reynolds et al. 2009). This is outlined in detail in Reynolds et al. (2009), but the principle argument is as follows: for every photon absorbed there must be a corresponding H-like photon liberated from the Fe atom. This corresponds to the Fe XXVI $K\alpha$ and $K\beta$ lines at 6.97 keV and 8.25 keV respectively. Since we have modeled the H-like and He-like lines as blends (both the Fe $K\alpha$ and Fe $K\beta$ regions), we cannot verify precisely whether enough flux is being re-emitted. However, it seems likely that $F_{\text{emi}} > F_{\text{abs}}$ based upon the flux of the 6.83 keV line, which is significantly greater than F_{abs} for both Model 1a and Model 1b, i.e., regardless of whether the absorption edge is narrow or smeared. This is physically consistent with at least some of the ionized photons originating from the same gaseous region that is absorbing the disk emission.

4. DISCUSSION AND CONCLUSIONS

We have performed a detailed spectral modeling analysis of five *NuSTAR* observations of V4641 Sgr during its 2021 outburst. The observations were spread over a month-long period, and we track the changes to its continuum and line features over this period. Our key findings are as follows:

- The broadband X-ray spectrum of V4641 Sgr in the soft states consists of a dominant bright multitemperature disk and a weak Comptonized component, with several ionized Fe K lines and an ionized Fe K edge component.
- The Fe K line fluxes correlate linearly with the disk continuum flux, and are quite stable in energy, consistent with the baseline near-neutral 6.4 keV Fe $K\alpha$ line, the ionized 6.7–7 keV Fe $K\alpha$ lines, and the ionized ~ 8 keV Fe $K\beta$ lines, modeled as three blended components.

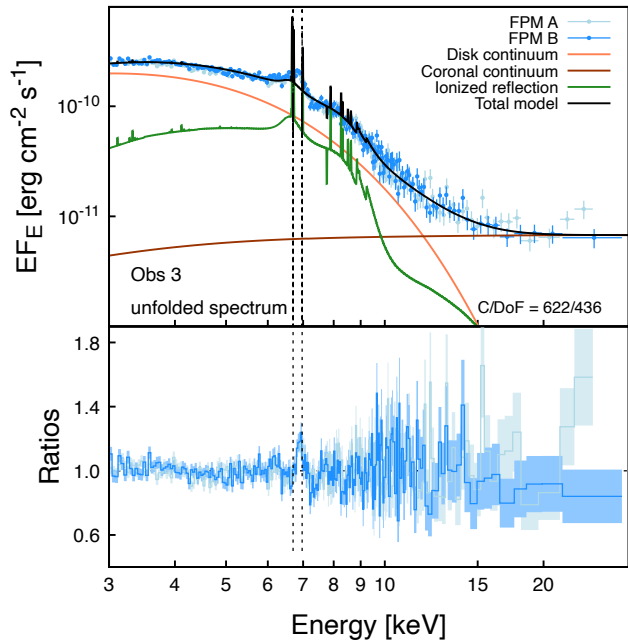


Figure 10. The unfolded *NuSTAR* spectrum and ratio residuals resulting from observation 3 (006) of V4641 Sgr fit with the model $\text{TBabs}^*(\text{diskbb}+\text{nthComp}+\text{xillverNS})$. The `xillverNS` component is an ionized reflection model which assumes an irradiating blackbody spectrum atop an infinite slab (accretion disk), given by a single-temperature blackbody continuum.

- We see an absorption edge component that is stable in energy and optical depth, interpreted as a highly ionized Fe K edge, which likely has some degree of smearing.

In the following subsections we discuss the implications of our spectral fitting results and offer further interpretations.

4.1. Reflection?

Given V4641 Sgr is in the soft spectral state, and there are clear signs of strong reprocessing in the form of ionized Fe K emission lines and an ionized Fe K edge with $\tau \sim 1$, it is worth asking the question, could the observed emission and absorption (edge) features simply be due to reflection off the accretion disk? Furthermore, and perhaps more pertinently, are we looking at just a single reprocessing region, or multiple (Shaw et al. 2022)?

Figure 10 shows a fit of the model $\text{TBabs}^*(\text{diskbb}+\text{nthComp}+\text{xillverNS})$ to *NuSTAR* observation 3 (006) of V4641 Sgr. The `xillverNS` component is a physically-motivated model, calculating reflection of an irradiating blackbody off an ionized slab (García et al. 2022). Our aim is to see if it can account for the three Gaussian line emission components and the continuum absorption edge at $\sim 9\text{--}10$ keV. We set

the blackbody temperature, kT_{bb} , equal to the inner disk temperature, kT_{in} , and allow the ionization, $\log \xi$, iron abundance, A_{Fe} , and inclination, i , of the reflector to vary freely.

There are a few key things to notice about this model fit (Figure 10). First, the reflection model adequately accounts for the smeared K edge. Second, the combined disk, power law, and reflection model fits well with the general phenomenological interpretation of a bright disk and a roughly flat, faint power law spectrum (just as is the case when we apply a smeared edge, the broadened dip inherent to the reflection component allows for a softer Comptonization component, as opposed to when we model the absorption feature as a sharp edge). Finally, and most interestingly, the reflection component cannot model all of the ionized line features. The fit accounts well for the near-neutral Fe K α emission at 6.4 keV and the ionized Fe K β emission at ~ 8 keV, but it fails to account for the strong ionized Fe K α line at 6.7–7 keV. We also tried including an additional reflected Comptonization component, `xillverCp` (García et al. 2014), thus adopting two reflection components, `xillverNS+xillverCp`. We found the observed power law flux is not sufficient to provide enough reflected flux to contribute significantly to the emission line features. This is further confirmation that we are quite likely viewing more than one photoionized region, or photoionized gas that has variable ionization—i.e. a single-zone photoionization model cannot account for all the emission lines simultaneously. The `relxillNS` model, i.e., the relativistic disk reflection version of `xillverNS`, does not yet contain the utility of an ionization gradient with disk radius (García et al. 2022). Such a model variant may be preferable to apply to these data, in order to reproduce emission lines from regions of differing ionization.

Shaw et al. (2022) also proposed multiple reprocessing regions to explain their *Chandra* grating spectra. They argued that the ionized Fe K emission likely originates from a single region, with the longer wavelength line species (from e.g., S/Ar, Si, Mg, and Ne) originating from a separate region. Unfortunately, they did not detect the 6.4 keV Fe K α line with enough statistical significance to model it with XSTAR. We suggest that in fact there are multiple Fe K emission regions, or at least, the reprocessing gas has a stratified ionization, but we cannot rule out the possibility that a more accurate continuum model may allow for improved modeling of the ionized lines. We discuss the details of the continuum emission in the following subsection.

4.2. Disk Continuum and Inner Radius

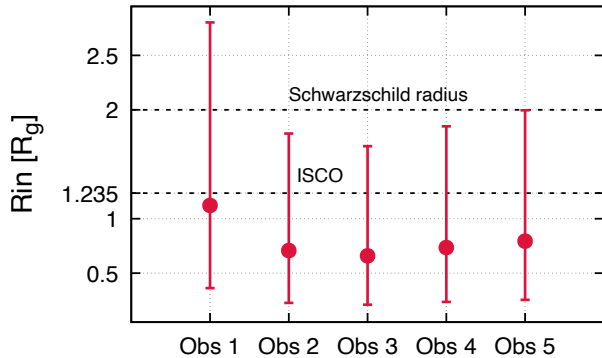


Figure 11. Constraints on the inner radius of the accretion disk resulting from joint fits of Model 1b to all five *NuSTAR* observations of V4641 Sgr (derived from the `diskbb` component). The error bars reflect the full range of possible R_{in} values based on the uncertainties on fit parameters (F_{disk} and T_{in}), binary characteristics (D , M_{BH} , and i), and color correction f_{col} .

The apparent inner radius of the observed accretion disk can be deduced from the measured disk flux (F_{disk}) and temperature (T_{in})—via the modeled `diskbb` component—through the following relation:

$$r_{\text{in}} = \left(\frac{F_{\text{disk}} D^2}{2(\cos i) \sigma T_{\text{in}}^4} \right)^{1/2}, \quad (1)$$

where $D = 6.2 \pm 0.7$ kpc is the distance to the source, and $i = 72 \pm 4$ deg is the disk inclination. The true disk inner radius, R_{in} , then depends on the proximity of the disk to the BH horizon (due to relativistic effects) and the degree of scattering in the disk atmosphere; the latter is primarily responsible for the decoupling of color temperature and effective temperature, which is parameterized by a color correction such that $R_{\text{in}} = f_{\text{col}} \cdot r_{\text{in}}$, with typical values of roughly $f_{\text{col}} \sim 1.5$ – 2 . The uncertainty on the inner disk radius can be impacted by the accuracy of the color correction factor. An additional caveat is that the `diskbb` model has an unphysical inner-boundary condition (it assumes a non-zero torque at the inner edge; Kubota et al. 1998; Zimmerman et al. 2005), which we do not account for here.

Figure 11 shows the R_{in} constraints resulting from the disk continuum fits to all five *NuSTAR* observations of V4641 Sgr. We use Equation 1 to calculate apparent inner radii, fold in the uncertainty in color correction ($f_{\text{col}} = 1.5 \pm 0.5$), and convert to $R_g = GM_{\text{BH}}/c^2$, adopting the full range of possible values of the fit parameters (F_{disk} , T_{in}) and system characteristics (D , i , M_{BH}), as opposed to propagating errors in quadrature, thus exploring the full uncertainty landscape. Most values lie within the Schwarzschild radius of the BH ($R_S = 2 R_g$), assuming a BH mass of $M_{\text{BH}} = 6.4 M_{\odot}$, and all have

valid (even preferred) solutions within the innermost stable circular orbit (ISCO) of a maximally spinning ($a_{\star} = 0.998$) BH. Most importantly, our results are consistent with the inner disk being outside the BH horizon and the ISCO.

We further tested the veracity of our inner radius constraints by replacing the `diskbb` component with a more physical disk continuum, `kerrbb`, which treats the relativistic effects to completion. If the fit results of Models 1a and 1b are valid, we should expect to find that `kerrbb` fits retrieve preferably higher spin values—this is indeed what we find. An exploration of the spin parameter space—via a `steppar` run of 50 steps in the range $0 \leq a_{\star} \leq 1$ —results in contours of increasing likelihood from low to high spins, i.e., maximal spin is strongly preferred.

A number of authors have inferred obscuration of the central engine based on the soft continuum of V4641 Sgr in its many outbursts (e.g., Revnivtsev et al. 2002; Maitra & Bailyn 2006; Koljonen & Tomsick 2020; Shaw et al. 2022), which appears faint enough such that the disk is unfeasibly small (i.e., within the BH horizon). The extent to which the continuum is obscured during the 2021 outburst, however, may be less extreme, as can be seen in Figure 11. We instead find solutions that are feasible, i.e., consistent with being outside the BH horizon and beyond the ISCO of a maximally spinning BH, despite the constraints skewing to low values. Since we are comparing results from observations of V4641 Sgr taken at various times across different outbursts, the contrasts may simply be due to intrinsic variations in the disk component. Thus, whilst we do see a hint of obscuration in the low intrinsic disk luminosity ($L_X \sim 0.003$ – $0.006 L_{\text{Edd}}$) and associated disk radius, the *NuSTAR* data alone do not allow us to disentangle a brighter, obscured component—i.e., via a partial covering model, as applied by Shaw et al. (2022) to the *Chandra*-HETG data—and an intrinsically faint disk.

4.3. Ionized Fe K edge: Column of the Photoionized Gas

We have shown in Sections 3.2 and 3.3 that the 2021 *NuSTAR* spectra of V4641 Sgr are best fit with the inclusion of a smeared edge component to model the absorption edge feature present in the data. This edge feature has been detected and interpreted before (Pahari et al. 2015; Shaw et al. 2022). Pahari et al. (2015) reported a strong, narrow edge feature at ~ 9.5 keV, and argued that it is a sharp Ni feature associated with a Ni emission line at ~ 8 keV. However, in the 2021 outburst, the energy of the edge aligns more closely with the K edges of highly-ionized Fe than Ni. Since our analysis shows that

a smeared edge at ~ 8.9 keV is preferred (Model 1b), we interpret the feature as the Fe XXV 8.83 keV continuum edge. It is worth noting that the degree of smearing applied to the edge, with a width of 2 keV at edge energy ~ 9 keV, implies a mildly relativistic Doppler shift. Since we do not see this degree of Doppler shifting to the observed emission lines, the smearing may be caused by photon scattering, rather than Doppler motions.

Furthermore, there is a statistical connection—an anti-correlation—between the width and the edge energy we have not fully explored in our analysis. Given that the increased sharpness of the feature yields a higher energy, this combined with the coarse spectral resolution of *NuSTAR* (relative to the energy separation of ionized Fe K continua) means the feature could comprise multiple ionized edges (e.g., both Fe XXV and Fe XXVI). The degree to which each ionization level contributes depends on *how* the gas is ionized, i.e., via radiative or collisional processes (see Kallman & Bautista 2001). A full treatment of relative ion fractions is far beyond the scope of this work.

We can use our constraints on the depth of this edge component to estimate the column density of the photoionized gas, given by $N_{\text{Fe}25} = \tau_{\text{edge}}/\sigma_{\text{Fe}25}$, where $\sigma_{\text{Fe}25}$ is the Fe XXV cross-section, which can be derived from tables provided by Verner et al. (1996). With $\sigma_{\text{Fe}25} = 1.956 \times 10^{-20}$ cm² and $\tau_{\text{edge}} = 0.89$ (from Table 1), the ionized Fe column density is $N_{\text{Fe}25} = 4.6 \times 10^{19}$ cm⁻². If we assume Solar abundances, ($A_{\text{Fe}} = 3.16 \times 10^{-5}$; Wilms et al. 2000), the photoionized gas has a hydrogen column density of $N_{\text{H}} = 1.4 \times 10^{24}$ cm⁻². This means we are seeing reprocessed emission from either one or more (see Section 4.1) photoionized region(s) that is mildly Compton thick but highly ionized, as opposed to a cold obscuring gas.

4.4. Conclusions

Through our detailed analysis of five *NuSTAR* spectral observations of the 2021 outburst of V4641 Sgr, we find several ionized Fe K emission lines and a smeared ionized Fe K edge. The line fluxes correlate strongly with the modeled intrinsic disk flux, and the smeared edge is stable in optical depth. Several of these features are well described by a single ionized reflection model, but additional ionized emission components remain, i.e., a single-zone, fixed ionization reflection model cannot explain all the features. Therefore we are likely viewing either multiple photoionized regions or a region with spatial variations in ionization.

Shaw et al. (2022) argued for significant partial obscuration of the central engine of V4641 Sgr based on

both the unfeasibly small inner disk radius derived from the disk continuum fit to their 2020 *NuSTAR* data, and the requirement for a partial covering to fit the *Chandra* spectrum down to low energies (below 1 keV). Similar arguments have been made based on modeling of previous observations of V4641 Sgr (Revnivtsev et al. 2002; Maitra & Bailyn 2006; Koljonen & Tomsick 2020). We see tentative evidence for obscuration of the disk based on its low intrinsic luminosity (and thus small inner radius, see Figure 11). On the other hand, while we cannot rule out the presence of a local partial covering, the strong correlation between the disk and line emission fluxes suggests that a significant portion of the disk emission that is reprocessed is also directly visible to us. We have shown, however, that reprocessing occurs within a highly ionized gas, which agrees with previous conclusions that scattering is taking place in either a large scale height disk or a wind (Koljonen & Tomsick 2020), possibly with a spherical geometry (Shaw et al. 2022).

Further characterization of the details of the continuum and ionized line and edge features in V4641 Sgr will require future observations with instruments with higher energy resolution alongside comparable broadband sensitivity, e.g., *XRISM* (Tashiro et al. 2018). The combination of *XRISM*'s Resolve and Xtend instruments would be ideal for a full characterization of the reprocessed emission we have modeled in this work, given the sensitivity out to ~ 25 keV and the incredible energy resolution (~ 4.5 eV at 6 keV). This combination will allow us to disentangle the complex ionized Fe emission lines and their relationship to the continuum, as well as identify velocity shifts. Measuring such shifts will facilitate further investigation of the smeared edge feature and bring us closer to understanding its origin and connection to the line features.

1 The authors extend their thanks to the anonymous ref-
 2 eree for their constructive comments which have helped
 3 turn this into a more complete piece of work.

4 RMTC and JN acknowledge support from NASA
 5 grant 80NSSC22K0330.

6 This research has made use of data, software and/or
 7 web tools obtained from the High Energy Astrophysics
 8 Science Archive Research Center (HEASARC), a service
 9 of the Astrophysics Science Division at NASA/GSFC
 10 and of the Smithsonian Astrophysical Observatory's
 11 High Energy Astrophysics Division.

12 This research has made use of ISIS functions (ISISs-
 13 cripts) provided by ECAP/Remeis observatory and MIT
 14 (<http://www.sternwarte.uni-erlangen.de/isis/>).

15 *Facilities:* *NuSTAR* (Harrison et al. 2013),
 16 HEASARC, HEASoft

17 *Software:* XSPEC v.12.13.1 (Arnaud 1996), ISIS
 18 v1.6.2-51 (Houck & Denicola 2000), XILLVER (García &
 19 Kallman 2010; García et al. 2013), RELXILL (v2.3; García
 20 et al. 2014; Dauser et al. 2014).

REFERENCES

- Arnaud, K. A. 1996, in *Astronomical Society of the Pacific Conference Series*, Vol. 101, *Astronomical Data Analysis Software and Systems V*, ed. G. H. Jacoby & J. Barnes, 17
- Bahramian, A., Altamirano, D., Heinke, C., et al. 2015, *The Astronomer's Telegram*, 7904, 1
- Brandt, W. N., & Schulz, N. S. 2000, *ApJL*, 544, L123, doi: [10.1086/317313](https://doi.org/10.1086/317313)
- Buisson, D. J. K., Neilsen, J., Motta, S., et al. 2021, *The Astronomer's Telegram*, 14992, 1
- Burrows, D. N., Hill, J. E., Nousek, J. A., et al. 2005, *SSRv*, 120, 165, doi: [10.1007/s11214-005-5097-2](https://doi.org/10.1007/s11214-005-5097-2)
- Coppi, P. S. 2000, in *AAS/High Energy Astrophysics Division*, Vol. 5, *AAS/High Energy Astrophysics Division #5*, 23.11
- Dauser, T., García, J., Parker, M. L., Fabian, A. C., & Wilms, J. 2014, *MNRAS*, 444, L100, doi: [10.1093/mnras/slu125](https://doi.org/10.1093/mnras/slu125)
- Díaz Trigo, M., Parmar, A. N., Boirin, L., Méndez, M., & Kaastra, J. S. 2006, *A&A*, 445, 179, doi: [10.1051/0004-6361:20053586](https://doi.org/10.1051/0004-6361:20053586)
- Done, C., Gierliński, M., & Kubota, A. 2007, *A&A Rv*, 15, 1, doi: [10.1007/s00159-007-0006-1](https://doi.org/10.1007/s00159-007-0006-1)
- Dunn, R. J. H., Fender, R. P., Körding, E. G., Belloni, T., & Cabanac, C. 2010, *MNRAS*, 403, 61, doi: [10.1111/j.1365-2966.2010.16114.x](https://doi.org/10.1111/j.1365-2966.2010.16114.x)
- Ebisawa, K. 1991, PhD thesis, JAXA, Institute of Space and Astronautical Science
- Fender, R., & Gallo, E. 2014, *SSRv*, 183, 323, doi: [10.1007/s11214-014-0069-z](https://doi.org/10.1007/s11214-014-0069-z)
- García, J., Dauser, T., Reynolds, C. S., et al. 2013, *ApJ*, 768, 146, doi: [10.1088/0004-637X/768/2/146](https://doi.org/10.1088/0004-637X/768/2/146)
- García, J., & Kallman, T. R. 2010, *ApJ*, 718, 695, doi: [10.1088/0004-637X/718/2/695](https://doi.org/10.1088/0004-637X/718/2/695)
- García, J., Dauser, T., Lohfink, A., et al. 2014, *ApJ*, 782, 76, doi: [10.1088/0004-637X/782/2/76](https://doi.org/10.1088/0004-637X/782/2/76)
- García, J. A., Dauser, T., Ludlam, R., et al. 2022, *ApJ*, 926, 13, doi: [10.3847/1538-4357/ac3cb7](https://doi.org/10.3847/1538-4357/ac3cb7)
- Gehrels, N., Chincarini, G., Giommi, P., et al. 2004, *ApJ*, 611, 1005, doi: [10.1086/422091](https://doi.org/10.1086/422091)
- Gendreau, K. C., Arzoumanian, Z., & Okajima, T. 2012, in *Society of Photo-Optical Instrumentation Engineers (SPIE) Conference Series*, Vol. 8443, *Space Telescopes and Instrumentation 2012: Ultraviolet to Gamma Ray*, ed. T. Takahashi, S. S. Murray, & J.-W. A. den Herder, 844313, doi: [10.1117/12.926396](https://doi.org/10.1117/12.926396)
- Gierliński, M., Zdziarski, A. A., Poutanen, J., et al. 1999, *MNRAS*, 309, 496, doi: [10.1046/j.1365-8711.1999.02875.x](https://doi.org/10.1046/j.1365-8711.1999.02875.x)

- Harrison, F. A., Craig, W. W., Christensen, F. E., et al. 2013, *Astrophys. J.*, 770, 103, doi: [10.1088/0004-637X/770/2/103](https://doi.org/10.1088/0004-637X/770/2/103)
- Hjellming, R. M., Rupen, M. P., Hunstead, R. W., et al. 2000, *ApJ*, 544, 977, doi: [10.1086/317255](https://doi.org/10.1086/317255)
- Homan, J., & Belloni, T. 2005, *Ap&SS*, 300, 107, doi: [10.1007/s10509-005-1197-4](https://doi.org/10.1007/s10509-005-1197-4)
- Homan, J., Neilsen, J., Allen, J. L., et al. 2016, *ApJL*, 830, L5, doi: [10.3847/2041-8205/830/1/L5](https://doi.org/10.3847/2041-8205/830/1/L5)
- Houck, J. C., & Denicola, L. A. 2000, in *Astronomical Society of the Pacific Conference Series*, Vol. 216, *Astronomical Data Analysis Software and Systems IX*, ed. N. Manset, C. Veillet, & D. Crabtree, 591
- in 't Zand, J., Heise, J., Bazzano, A., Cocchi, M., & Smith, M. J. S. 1999, *IAUC*, 7243, 2
- in't Zand, J. J. M., Kuulkers, E., Bazzano, A., et al. 2000, *A&A*, 357, 520, doi: [10.48550/arXiv.astro-ph/0001110](https://doi.org/10.48550/arXiv.astro-ph/0001110)
- Joye, W. A., & Mandel, E. 2003, in *Astronomical Society of the Pacific Conference Series*, Vol. 295, *Astronomical Data Analysis Software and Systems XII*, ed. H. E. Payne, R. I. Jedrzejewski, & R. N. Hook, 489
- Kallman, T., & Bautista, M. 2001, *ApJS*, 133, 221, doi: [10.1086/319184](https://doi.org/10.1086/319184)
- King, A. L., Miller, J. M., Raymond, J., Reynolds, M. T., & Morningstar, W. 2015, *ApJL*, 813, L37, doi: [10.1088/2041-8205/813/2/L37](https://doi.org/10.1088/2041-8205/813/2/L37)
- Koljonen, K. I. I., & Tomsick, J. A. 2020, *A&A*, 639, A13, doi: [10.1051/0004-6361/202037882](https://doi.org/10.1051/0004-6361/202037882)
- Kubota, A., Tanaka, Y., Makishima, K., et al. 1998, *PASJ*, 50, 667, doi: [10.1093/pasj/50.6.667](https://doi.org/10.1093/pasj/50.6.667)
- Lee, J. C., Reynolds, C. S., Remillard, R., et al. 2002, *ApJ*, 567, 1102, doi: [10.1086/338588](https://doi.org/10.1086/338588)
- Li, L.-X., Zimmerman, E. R., Narayan, R., & McClintock, J. E. 2005, *The Astrophysical Journal Supplement Series*, 157, 335, doi: [10.1086/428089](https://doi.org/10.1086/428089)
- MacDonald, R. K. D., Bailyn, C. D., Buxton, M., et al. 2014, *ApJ*, 784, 2, doi: [10.1088/0004-637X/784/1/2](https://doi.org/10.1088/0004-637X/784/1/2)
- Maitra, D., & Bailyn, C. D. 2006, *ApJ*, 637, 992, doi: [10.1086/498422](https://doi.org/10.1086/498422)
- Makishima, K., Maejima, Y., Mitsuda, K., et al. 1986, *ApJ*, 308, 635, doi: [10.1086/164534](https://doi.org/10.1086/164534)
- Matsuoka, M., Kawasaki, K., Ueno, S., et al. 2009, *PASJ*, 61, 999, doi: [10.1093/pasj/61.5.999](https://doi.org/10.1093/pasj/61.5.999)
- Mihara, T., Nakajima, M., Sugizaki, M., et al. 2011, *PASJ*, 63, S623, doi: [10.1093/pasj/63.sp3.S623](https://doi.org/10.1093/pasj/63.sp3.S623)
- Miller, J. M., Raymond, J., Homan, J., et al. 2006, *ApJ*, 646, 394, doi: [10.1086/504673](https://doi.org/10.1086/504673)
- Miller, L., Turner, T. J., & Reeves, J. N. 2008, *A&A*, 483, 437, doi: [10.1051/0004-6361:200809590](https://doi.org/10.1051/0004-6361:200809590)
- Mitsuda, K., Inoue, H., Koyama, K., et al. 1984, *PASJ*, 36, 741
- Motta, S., Kuulkers, E., Sanchez-Fernandez, C., et al. 2021, *The Astronomer's Telegram*, 14971, 1
- Muñoz-Darias, T., Motta, S., & Belloni, T. M. 2011, *MNRAS*, 410, 679, doi: [10.1111/j.1365-2966.2010.17476.x](https://doi.org/10.1111/j.1365-2966.2010.17476.x)
- Muñoz-Darias, T., Torres, M. A. P., & Garcia, M. R. 2018, *MNRAS*, 479, 3987, doi: [10.1093/mnras/sty1711](https://doi.org/10.1093/mnras/sty1711)
- Muñoz-Darias, T., Casares, J., Mata Sánchez, D., et al. 2016, *Nature*, 534, 75, doi: [10.1038/nature17446](https://doi.org/10.1038/nature17446)
- Negoro, H., Nakajima, M., Mihara, T., et al. 2021, *The Astronomer's Telegram*, 14968, 1
- Neilsen, J., & Lee, J. C. 2009, *Nature*, 458, 481, doi: [10.1038/nature07680](https://doi.org/10.1038/nature07680)
- Orosz, J. A., Kuulkers, E., van der Klis, M., et al. 2001, *ApJ*, 555, 489, doi: [10.1086/321442](https://doi.org/10.1086/321442)
- Pahari, M., Misra, R., Dewangan, G. C., & Pawar, P. 2015, *ApJ*, 814, 158, doi: [10.1088/0004-637X/814/2/158](https://doi.org/10.1088/0004-637X/814/2/158)
- Ponti, G., Bianchi, S., Muñoz-Darias, T., et al. 2016, *Astronomische Nachrichten*, 337, 512, doi: [10.1002/asna.201612339](https://doi.org/10.1002/asna.201612339)
- Ponti, G., Fender, R. P., Begelman, M. C., et al. 2012, *MNRAS*, 422, L11, doi: [10.1111/j.1745-3933.2012.01224.x](https://doi.org/10.1111/j.1745-3933.2012.01224.x)
- Remillard, R. A., & McClintock, J. E. 2006, *ARA&A*, 44, 49, doi: [10.1146/annurev.astro.44.051905.092532](https://doi.org/10.1146/annurev.astro.44.051905.092532)
- Revnivtsev, M., Gilfanov, M., Churazov, E., & Sunyaev, R. 2002, *A&A*, 391, 1013, doi: [10.1051/0004-6361:20020865](https://doi.org/10.1051/0004-6361:20020865)
- Reynolds, C. S., Fabian, A. C., Brenneman, L. W., et al. 2009, *MNRAS*, 397, L21, doi: [10.1111/j.1745-3933.2009.00676.x](https://doi.org/10.1111/j.1745-3933.2009.00676.x)
- Sadowski, A., Abramowicz, M., Bursa, M., et al. 2011, *A&A*, 527, A17, doi: [10.1051/0004-6361/201015256](https://doi.org/10.1051/0004-6361/201015256)
- Shaw, A. W., Miller, J. M., Grinberg, V., et al. 2022, *MNRAS*, 516, 124, doi: [10.1093/mnras/stac2213](https://doi.org/10.1093/mnras/stac2213)
- Smith, D. A., Levine, A. M., & Morgan, E. H. 1999, *The Astronomer's Telegram*, 43, 1
- Tashiro, M., Maejima, H., Toda, K., et al. 2018, in *Society of Photo-Optical Instrumentation Engineers (SPIE) Conference Series*, Vol. 10699, *Space Telescopes and Instrumentation 2018: Ultraviolet to Gamma Ray*, ed. J.-W. A. den Herder, S. Nikzad, & K. Nakazawa, 1069922, doi: [10.1117/12.2309455](https://doi.org/10.1117/12.2309455)
- Tetarenko, B. E., Sivakoff, G. R., Heinke, C. O., & Gladstone, J. C. 2016, *ApJS*, 222, 15, doi: [10.3847/0067-0049/222/2/15](https://doi.org/10.3847/0067-0049/222/2/15)
- Ueda, Y., Murakami, H., Yamaoka, K., Dotani, T., & Ebisawa, K. 2004, *ApJ*, 609, 325, doi: [10.1086/420973](https://doi.org/10.1086/420973)
- Verner, D. A., Ferland, G. J., Korista, K. T., & Yakovlev, D. G. 1996, *ApJ*, 465, 487, doi: [10.1086/177435](https://doi.org/10.1086/177435)

- Wilms, J., Allen, A., & McCray, R. 2000, *ApJ*, 542, 914, doi: [10.1086/317016](https://doi.org/10.1086/317016)
- Winkler, C., Courvoisier, T. J. L., Di Cocco, G., et al. 2003, *A&A*, 411, L1, doi: [10.1051/0004-6361:20031288](https://doi.org/10.1051/0004-6361:20031288)
- Zdziarski, A. A., Johnson, W. N., & Magdziarz, P. 1996, *MNRAS*, 283, 193, doi: [10.1093/mnras/283.1.193](https://doi.org/10.1093/mnras/283.1.193)
- Zdziarski, A. A., Szanecki, M., Poutanen, J., Gierliński, M., & Biernacki, P. 2020, *MNRAS*, 492, 5234, doi: [10.1093/mnras/staa159](https://doi.org/10.1093/mnras/staa159)
- Zimmerman, E. R., Narayan, R., McClintock, J. E., & Miller, J. M. 2005, *ApJ*, 618, 832, doi: [10.1086/426071](https://doi.org/10.1086/426071)
- Życki, P. T., Done, C., & Smith, D. A. 1999, *MNRAS*, 309, 561, doi: [10.1046/j.1365-8711.1999.02885.x](https://doi.org/10.1046/j.1365-8711.1999.02885.x)